Supplementary Information: Versatile Control of Nonlinear Topological States in Non-Hermitian Systems

Zhao-Fan Cai,[1] Yu-Chun Wang,[1] Yu-Ran Zhang,[1] Tao Liu,[1,*] and Franco Nori[2,3]

[1]*School of Physics and Optoelectronics, South China University of Technology, Guangzhou 510640, China*

[2]*Center for Quantum Computing, RIKEN, Wakoshi, Saitama 351-0198, Japan*

[3]*Department of Physics, University of Michigan, Ann Arbor, Michigan 48109-1040, USA*

(Dated: August 14, 2025)

Supplementary Note 1: POSSIBLE EXPERIMENTAL SETUP

The non-Hermitian nonlinear lattices considered in this work can be feasibly implemented across a variety of experimental platforms, including photonic systems[1,2] and electronic circuits[3–5]. Here, we focus on an electronic circuit platform that allows for both tunable nonreciprocal hopping[6–8] and controllable nonlinearity[3–5]. In particular, the key ingredients of our model, i.e., nonreciprocal hopping and amplitude-dependent nonlinear hopping, can be effectively realized within this platform. In the following, we provide a detailed description of the circuit implementation of each hopping mechanism.

(i) The nonreciprocal hopping between neighboring nodes is implemented using negative impedance converter (INIC) circuits, which introduce direction-dependent current inversion[6,8], as illustrated in Fig. S1(a). In this configuration, each pair of adjacent nodes is connected via a capacitor C_1 and an INIC. The INIC efficiently introduces an asymmetric capacitive coupling, exhibiting an equivalent capacitance of $\pm C_2$ depending on the direction of signal flow.

(ii) The nonlinear hopping between neighboring nodes is realized by utilizing a nonlinear capacitor[3], as shown in Fig. S1(b). Specifically, we consider an interaction between two resonators coupled via a linear capacitor $C_{\rm L}$ and a nonlinear capacitor $C_{\rm NL}$. Following the derivation[3], the dynamics of the system can be modeled using coupled-mode equations:

$$-j\frac{da_1}{dt} = \omega_0 a_1 + [\kappa + \nu(|V_{C_1} - V_{C_2}|)]a_2, \tag{S1}$$

$$-j\frac{da_2}{dt} = \omega_0 a_2 + [\kappa + \nu(|V_{C_1} - V_{C_2}|)]a_1, \tag{S2}$$

where ω_0 is the resonance frequency, and the couplings consist of a linear term $\kappa = C_{\rm L}/(C_1 + C_2)$ and a nonlinear term $\nu(V) = C_{\rm NL}(|V_{C_1} - V_{C_2}|)/(C_1 + C_2)$, which depends on the voltage difference across the nonlinear capacitor. This structure

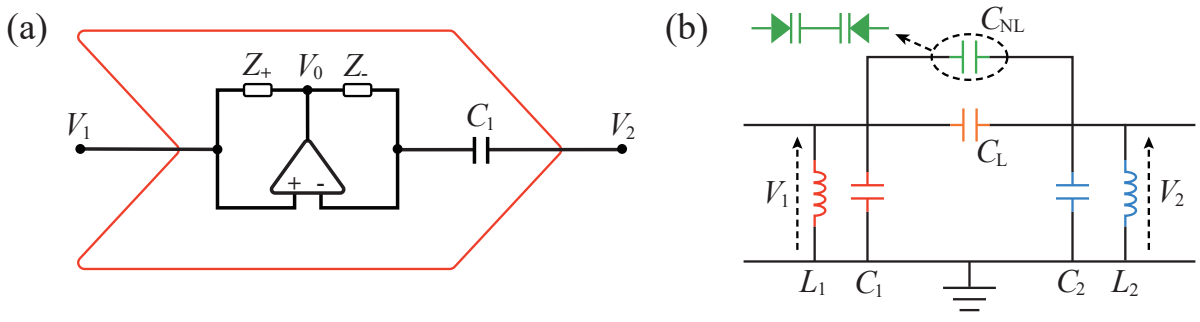

FIG. S1. (a) Experimental circuit realization of nonreciprocal hopping between two neighbor nodes via the negative impedance converters through current inversion (INIC), which consists of capacitor, resistor and operational amplifier. (b) Experimental circuit realization of nonlinear hopping, which consists of two shut LC resonators, a linear capacitor $C_{\rm L}$ and a nonlinear capacitor $C_{\rm NL}$.

allows the coupling strength to be modulated dynamically by the local voltage amplitude, thus realizing an effective nonlinear hopping mechanism. Note that different forms of amplitude-dependent nonlinear coupling between two nodes have also been realized in circuit platforms[4,5]. In addition, amplitude-dependent coupling can be implemented in optical systems using nonlinear fibers[1,2], where the coupling strength varies with the light intensity.

Supplementary Note 2: IN-GAP NON-ZERO MODES

In the main text, we discuss the delocalization of in-gap topological zero modes (TZMs). Beyond these in-gap TZMs, the nonlinearity can also induce in-gap non-zero modes with eigenvalues that are not fixed at zero frequency. In this section, we provide details on the wavefunction distributions of these in-gap non-zero modes within the nonlinear eigenfrequency spectrum.

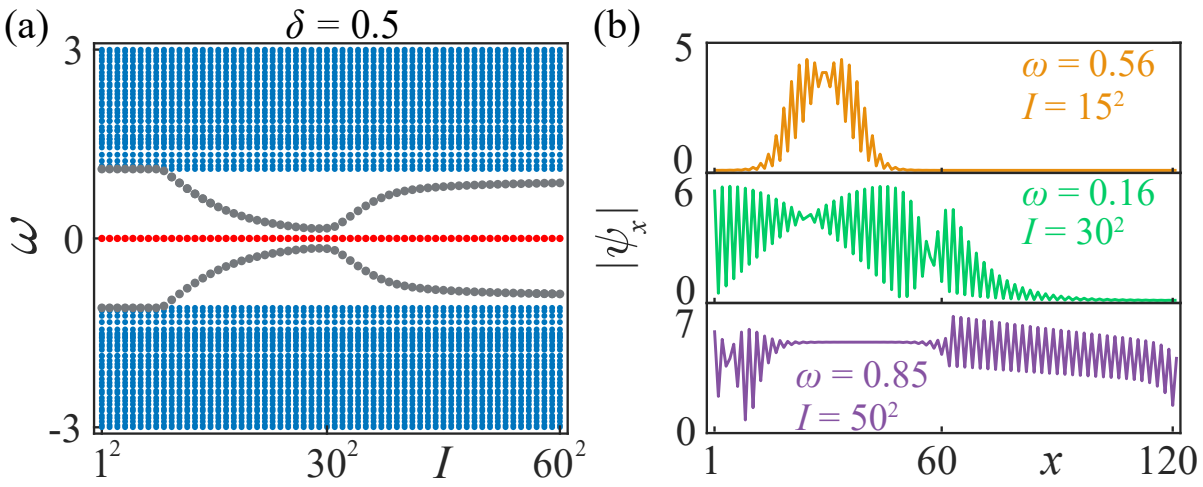

FIG. S2. (a) Eigenfrequency spectrum ω versus $I = \sum_j (|a_j|^2 + |b_j|^2)$ for $\delta = 0.5$, where the gray dots denotes the in-gap non-zero modes and red dots mark the TZMs. The corresponding spatial distributions $|\psi_x|$ of typical in-gap non-zero modes for different I are shown in (b). The parameters used are $J = 1.5$, $\tau = \tilde{\lambda}_j = t_\mathrm{d} = 2.5$, $\tilde{t}_j = 1.0$, $\alpha = 0.05$, $\beta = 0$, $N = 31$, and $L = 121$.

Figure S2 shows the eigenfrequency spectrum ω versus $I = \sum_j (|a_j|^2 + |b_j|^2)$, and the corresponding spatial distributions $|\psi_x|$ of the in-gap non-zero modes [light black dots in Fig. S2(a)] for $\delta = 0.5$ with $\alpha = 0.05$ and $\beta = 0$. The in-gap non-zero modes emerge only when I exceeds a certain value, and their eigenvalues exhibit a strong dependence on I. Furthermore, as shown in Fig. S2(a), the in-gap non-zero modes originates from the bulk modes. When I is small, the in-gap non-zero modes are mainly localized at the Hermitian nonlinear chain. As I increases, the in-gap non-zero modes become extended, while the wavefunction profiles remain undefined or arbitrary in shape, as shown in Fig. S2(b). Due to the undefined waveform and unconstrained eigenvalues of the in-gap non-zero modes for different I, in this work we focus exclusively on the TZMs.

Supplementary Note 3: EFFECTS OF DISORDER ON THE DELOCALIZED TZMS FOR $\delta = \delta_\mathrm{c}$ AND $\beta = 0$

As demonstrated in the main text, for $\delta = \delta_\mathrm{c}$ and $\beta = 0$, the TZM becomes delocalized, and can occupy both the entire Hermitian and non-Hermitian lattices due to the interplay of nonlinearity, the non-Hermitian skin effect (NHSE), and topology. Here, we discuss the robustness of the TZM wavefunction delocalization against disorder due to topological protection.

We investigate two types of random disorders, i.e., disordered on-site energy, $\hat{\mathcal{H}}_1$, and disordered hopping strength, $\hat{\mathcal{H}}_2$, each

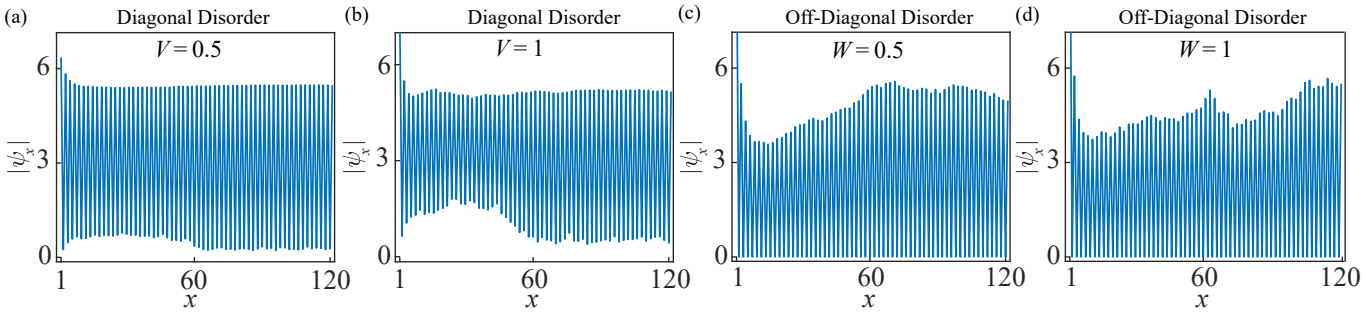

FIG. S3. Spatial distributions $|\psi_x|$ of the delocalized TZM subject to a disordered onsite potential (a,b) and a disordered hopping (c,d) for $\delta = \delta_c = 1.0$, $\alpha = 0.05$ and $I = 43^2$. The disordered onsite potential (i.e., diagonal disorder) and disordered hopping (i.e., off-diagonal disorder) are randomly sampled within the respective ranges of $[-V/2,\ V/2]$ and $[-W/2,\ W/2]$, respectively. The other parameters used here are $J = 1.5$, $\beta = 0$, $\tau = \tilde{\lambda}_j = t_d = 2.5$, $\tilde{t}_j = 1.0$, $N = 31$, and $L = 121$.

applied separately to the topological interface model. The disordered Hamiltonian is written as $\hat{\mathcal{H}}_{\text{dis}} = \hat{\mathcal{H}} + \hat{\mathcal{H}}_j$ $(j = 1, 2)$, with

$$\begin{aligned}\hat{\mathcal{H}} = &\sum_{j\le N} \left(\tau \left|a_j\right\rangle \left\langle b_j\right| + t_{j-1} \left|a_j\right\rangle \left\langle b_{j-1}\right| + \text{H.c.}\right) + \sum_{j>N} \left[(J-\delta) \left|a_j\right\rangle \left\langle b_j\right| + (J+\delta) \left|b_j\right\rangle \left\langle a_j\right|\right] \\ &+ \sum_{j>N} \left(\lambda_j \left|a_{j+1}\right\rangle \left\langle b_j\right| + \text{H.c.}\right) + t_d \left(\left|a_{N+1}\right\rangle \left\langle b_N\right| + \text{H.c.}\right), \end{aligned} \tag{S3}$$

$$\hat{\mathcal{H}}_1 = \sum_j \left(V_{a,j} \left|a_j\right\rangle \left\langle a_j\right| + V_{b,j} \left|b_j\right\rangle \left\langle b_j\right|\right), \tag{S4}$$

$$\hat{\mathcal{H}}_2 = \sum_j \left(W_{1,j} \left|a_j\right\rangle \left\langle b_j\right| + W_{2,j} \left|a_{j+1}\right\rangle \left\langle b_j\right| + \text{H.c.}\right), \tag{S5}$$

where the disordered onsite potential $V_{a,j}$ and $V_{b,j}$ (i.e., diagonal disorder) and the disordered hopping $W_{1,j}$ and $W_{2,j}$ (i.e., off-diagonal disorder) are randomly sampled within the respective ranges of $[-V/2,\ V/2]$ and $[-W/2,\ W/2]$, respectively.

Figure S3 shows the spatial distributions $|\psi_x|$ of the delocalized TZM subject to the disordered onsite potential (a,b) and the disordered hopping (c,d) for $\delta = \delta_c = 1.0$, $\alpha = 0.05$ and $I = 43^2$. The TZM remains extended even under strong disorder, demonstrating the robustness of topological protection in TZMs, even in the presence of strong nonlinear effects.

Supplementary Note 4: WAVEFUNCTION PROFILES OF TZMS FOR DIFFERENT KERR NONLINEAR COEFFICIENTS β AND NONRECIPROCAL HOPPING AMPLITUDE δ

This section provides a detailed exploration of the nonlinearity-driven control of TZMs. We begin by now presenting the nonlinear eigenequation for a TZM with zero eigenfrequency, $\omega = 0$, expressed as

$$\tau a_j + \left(\tilde{t}_j + \alpha a_{j+1}^2\right) a_{j+1} = 0, \quad j < N, \tag{S6}$$

$$\tau a_N + t_d a_{N+1} = 0, \quad j = N, \tag{S7}$$

$$(J+\delta) a_j + \left(\tilde{\lambda}_j + \beta a_{j+1}^2\right) a_{j+1} = 0, \quad j > N, \tag{S8}$$

and $b_j = 0$. We now focus on parameters that deviate from the linear critical condition $\delta_c = \lambda - J$ below, and begin by examining the case where $\tilde{t}_j = t$ and $\tilde{\lambda}_j = \lambda$ are constants. To this end, we consider the case where the Hermitian chain is in the topological trivial regime with $\tau > t$, and the non-Hermitian chain in the topological nontrivial regime, with $J \in [-\sqrt{\delta^2+\lambda^2},\ \sqrt{\delta^2+\lambda^2}]$ for $|\lambda| \geq |\delta|$, when $\beta = 0$[9]. Without loss of generality, we further assume $(J+\delta) > \lambda$.

Figure S4 plots spatial distributions $|\psi_x|$ of the TZMs under various values of I, β and δ. According to Eqs. (S6)-(S8), we can infer that the TZM is exponentially localized at the right boundary due to the NHSE when the nonlinear intensity I is small, as indicated by the black lines in Fig. S4. As I increases, the nonlinear term $\tilde{\lambda}_j + \beta a_{j+1}^2$ in Eq. (S8) grows accordingly. This

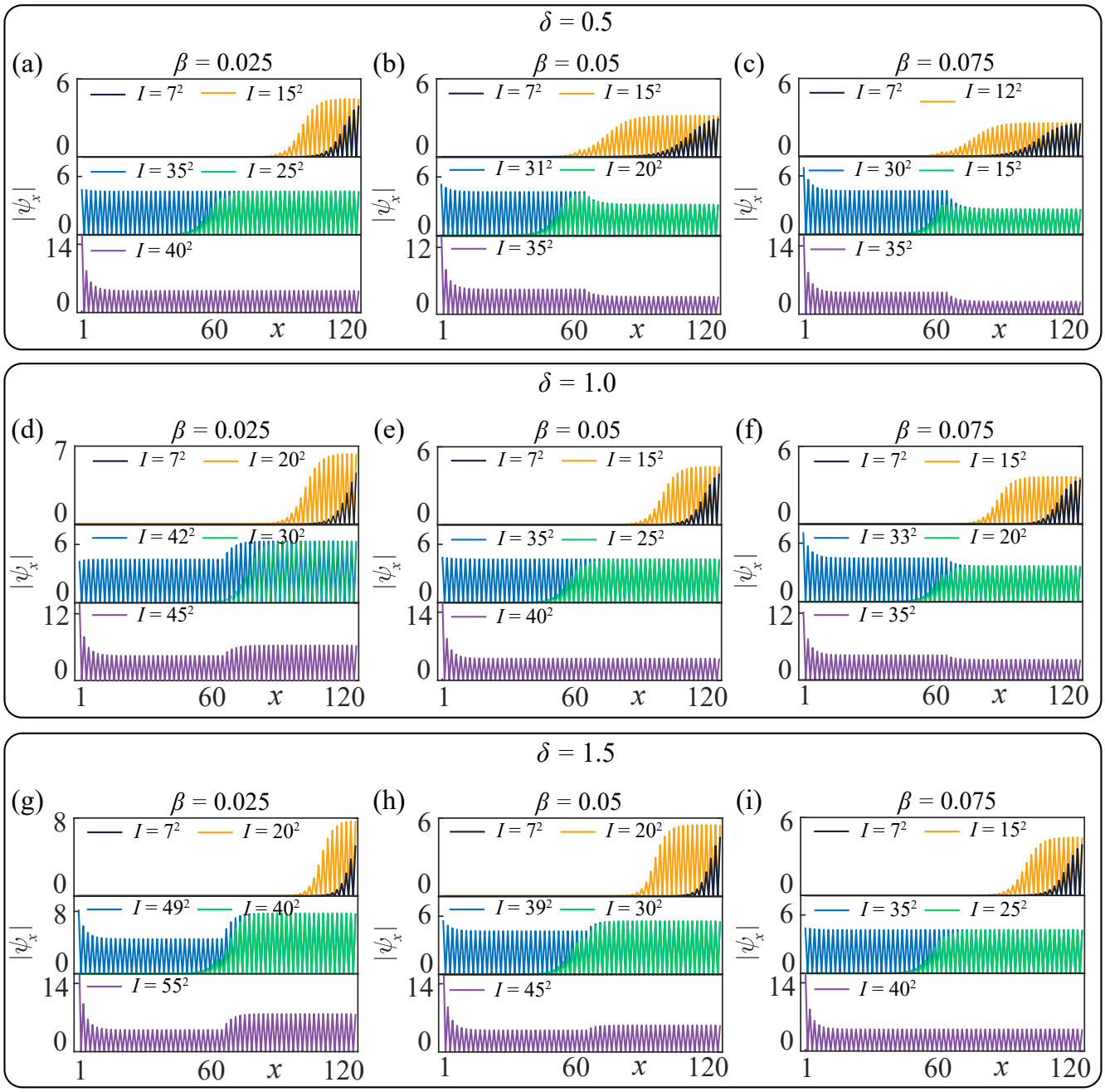

FIG. S4. Spatial distributions $|\psi_x|$ of the TZMs under various values of I and the Kerr coefficient β for (a-c) $\delta = 0.5$, (d-f) $\delta = 1.0$, and (g-i) $\delta = 1.5$. Other parameters used here are $J = 1.5$, $\alpha = 0.05$, $\tilde{t}_j = \tilde{\lambda}_j = 1.5$, $\tau = t_d = 2.5$, $N = 31$, and $L = 121$.

behavior, when analyzed through Eqs. (S6)–(S8), suggests that the wavefunction of the TZM gradually extends from the right boundary into the bulk, progressively occupying more bulk sites. This transition is illustrated by the numerical results shown by the orange and green lines in Fig. S4. Eventually, under strong nonlinear intensity I, the TZM extends to occupy the entire lattice of the interface model, forming either one or two plateaus depending on the values of δ and β, as illustrated by the blue lines in Fig. S4. When I is further increased beyond this threshold value, the wavefunctions become concentrated at the left end of the chain, while the plateaus are maintained (see purple lines in Fig. S4). Moreover, using Eqs. (S6)-(S8), we can infer that the spatial distribution $|\psi_x|$ of the TZM should remain flat across the lattice, except near the interface, because any significant deviation from this flatness would cause the wavefunction to diverge in the thermodynamic limit.

Based on the above discussion, in the bulk regime under strong nonlinearity, the spatial distribution of the TZM tends to become uniform along each chain. Therefore, by applying Eqs. (S6)–(S8), the plateau heights in the bulk regimes of the non-Hermitian and Hermitian chains can be derived as follows: for $j > N$, the state amplitude of the TZM is $|a_{\rm R}| = \sqrt{(J+\delta-\lambda)/\beta}$, and for $j < N$, the state amplitude of the TZM is $|a_{\rm L}| = \sqrt{(\tau-t)/\alpha}$, respectively. By varying β for different values of δ, the relative plateau heights between the Hermitian and non-Hermitian chains can be tuned flexibly (see Fig. S4). Specifically, by choosing δ and β such that $|a_{\rm L}| = |a_{\rm R}|$, a uniform plateau across the entire lattice can be achieved.

Supplementary Note 5: DETAILS ON ARBITRARY DESIGN OF WAVEFUNCTION PROFILES OF TZMS

For constant values of $\tilde{t}_j$ and $\tilde{\lambda}_j$, we can obtain a flat wavefunction profile of the TZM across the entire lattice. As demonstrated in the main text, the wavefunction profiles across the lattice can be designed arbitrarily. In this section, we provide detailed descriptions of the distributions of $\tilde{t}_j$ and $\tilde{\lambda}_j$ for wavefunction profiles with square, isosceles triangle, and cosine shapes. Additionally, we examine the impact of disorder on these distributions.

A. Arbitrary wavefunction profile by engineering the hopping energies $\tilde{t}_j$ and $\tilde{\lambda}_j$

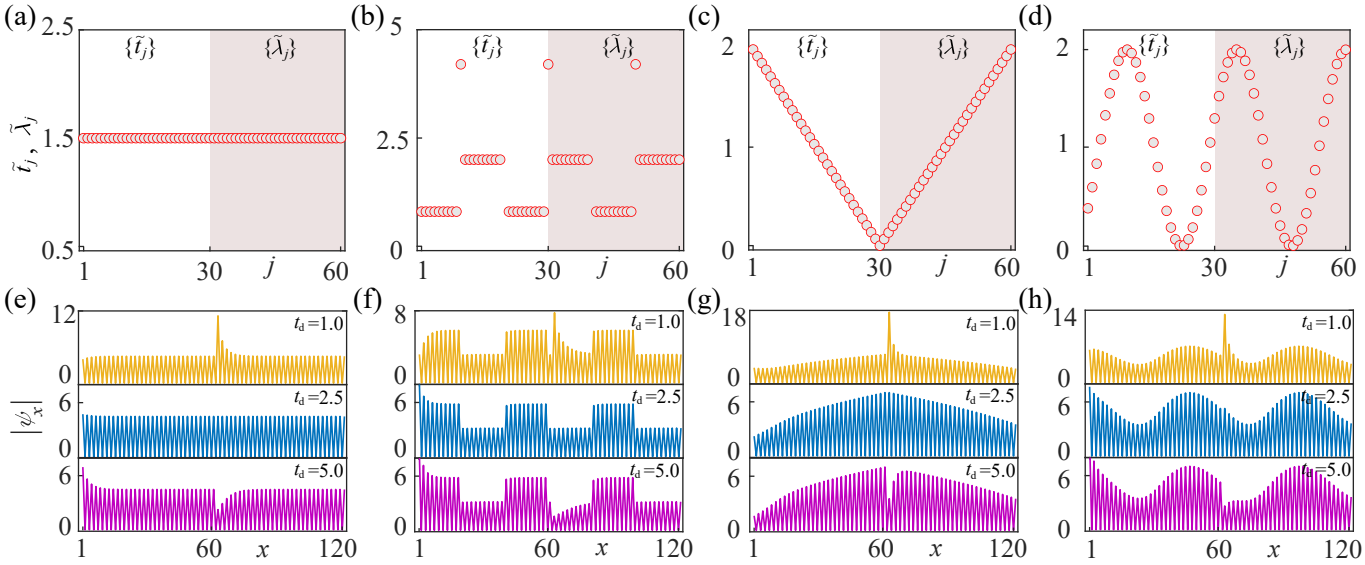

FIG. S5. (a-d) Distributions of the hopping energies $\tilde{t}_j$ and $\tilde{\lambda}_j$ used to create flat, square, isosceles triangle, and cosine-shaped wavefunction profiles, respectively. Unfilled and filled regions correspond to the Hermitian and non-Hermitian regimes of the chains. The spatial distributions $|\psi_x|$ of the TZMs are shown in (e-h), where the extended wavefunctions exhibit (e) a flat profile, (f) a square profile, (g) an isosceles triangle profile, and (h) a cosine profile. The state amplitude of the TZM around the interface sites can be tuned by adjusting the inter-chain coupling strength $t_{\rm d}$ [see each row in (e-h)]. Other parameters used here are $J = 1.5$, $\delta = 1.0$, $\alpha = \beta = 0.05$, $\tau = 2.5$, $N = 31$ and $L = 121$.

The wavefunction profiles of the extended TZMs across the entire lattice can be freely designed by engineering distributions of $\tilde{t}_j$ and $\tilde{\lambda}_j$. Figure S5(a-d) illustrates the distributions of $\tilde{t}_j$ and $\tilde{\lambda}_j$ employed to generate flat, square, isosceles triangle, and cosine-shaped wavefunction profiles[10], respectively. The spatial distributions $|\psi_x|$ of the TZMs are shown in S5(e-h), where the extended wavefunctions exhibit (e) a flat profile, (f) a square profile, (g) an isosceles triangle profile, and (h) a cosine profile. The state amplitude of the TZM around the interface sites can be tuned by adjusting the inter-chain coupling strength $t_{\rm d}$ [see each row in (e-h)]. Specifically, at the interface site, we have $|a_{N+1}| = \tau|a_N|/t_d$, which satisfies $|a_{N+1}| > |a_N|$ for $t_{\rm d} < \tau$ and $|a_{N+1}| < |a_N|$ for $t_{\rm d} > \tau$, as manifested in Fig. S5(e-h).

B. Effect of disorder on arbitrarily-designed wavefunction profiles

To demonstrate the robustness of arbitrarily-designed wavefunction profiles for the TZMs across the entire lattice under the influence of disorder, we introduce random perturbations to the hopping energies. The hopping energies are modified as $\tilde{t}_j \to \tilde{t}_j(1+W_j)$, and $\tilde{\lambda}_j \to \tilde{\lambda}_j(1+V_j)$, where W_j and V_j are independent random variables uniformly distributed over the range $[-W/2,\ W/2]$. Here, W quantifies the disorder strength, providing a controlled parameter to evaluate the stability and resilience of the wavefunction profiles against spatially distributed random disorder.

Figure S6 illustrates the spatial distributions $|\psi_x|$ of the TZMs for wavefunction profiles with shapes (a) flat, (b) square, (c) isosceles triangle, and (d) cosine, both in the absence of disorder (blue lines) and in the presence of disorder (red circles). The disordered state distributions show negligible deviations from the unperturbed ones, highlighting the remarkable robustness of the designed TZMs against disorder due to their topological nature.

Supplementary Note 6: SPECTRAL LOCALIZER IN THE NONLINEAR NON-HERMITIAN SYSTEM

In the main text, we present the local band gap μ_ζ and the local topological invariant C_ζ for the flat-shaped TZMs. Here, we discuss the topological properties of the cosine-shaped TZMs.

Figure S7(a-d) shows the spatial distribution $|\psi_x|$ of the TZM (upper panel) and their transformed counterparts $\left|\bar{\psi}_x\right| = \left|\hat{S}\left|\psi\right\rangle\right|$ under a similarity transformation (lower panel) for different I. The extended cosine-shaped TZM across the entire lattice is observed as the nonlinear intensity I increases. We then calculate the site-resolved eigenvalues $\sigma(\tilde{L}_\zeta)$ of the reduced spectral localizer $\tilde{L}_\zeta$ for $\bar{\omega} = 0$ using the similarity-transformed Hamiltonian $\hat{\mathcal{H}}_{\rm S}$, as shown in Fig. S7(e-h). The spectrum $\sigma(\tilde{L}_\zeta)$ crosses the zero energy line (black dotted line), as indicated by the red curves. The site-resolved local gap μ_ζ (upper panels) and

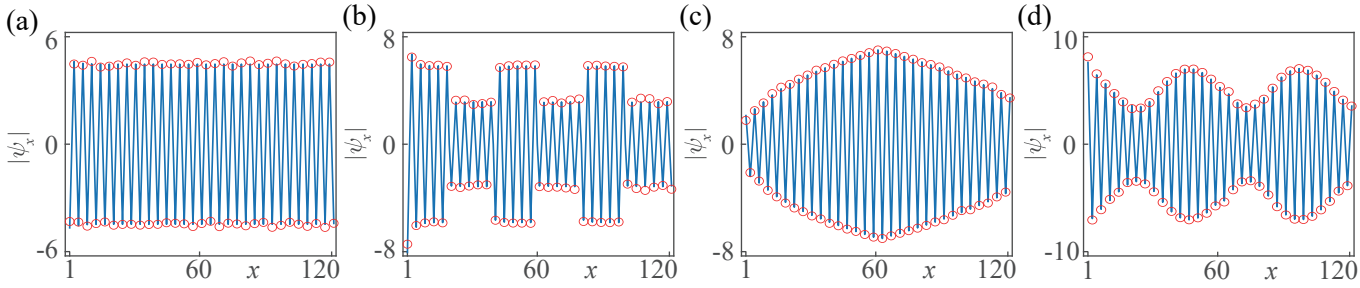

FIG. S6. Spatial distributions $|\psi_x|$ of the TZMs for wavefunction profiles with (a) flat, (b) square, (c) isosceles triangle, and (d) cosine shapes, subject to random disorder applied to the hopping energies $\tilde{t}_j \to \tilde{t}_j(1+W_j)$ and $\tilde{\lambda}_j \to \tilde{\lambda}_j(1+V_j)$. The blue lines indicate the state distributions without perturbation, while the red circles depict the distributions in the presence of disorder. Other parameters used are $J = 1.5$, $\delta = 1.0$, $W = 0.2$, $\alpha = \beta = 0.05$, $\tau = t_{\rm d} = 2.5$, $N = 31$ and $L = 121$.

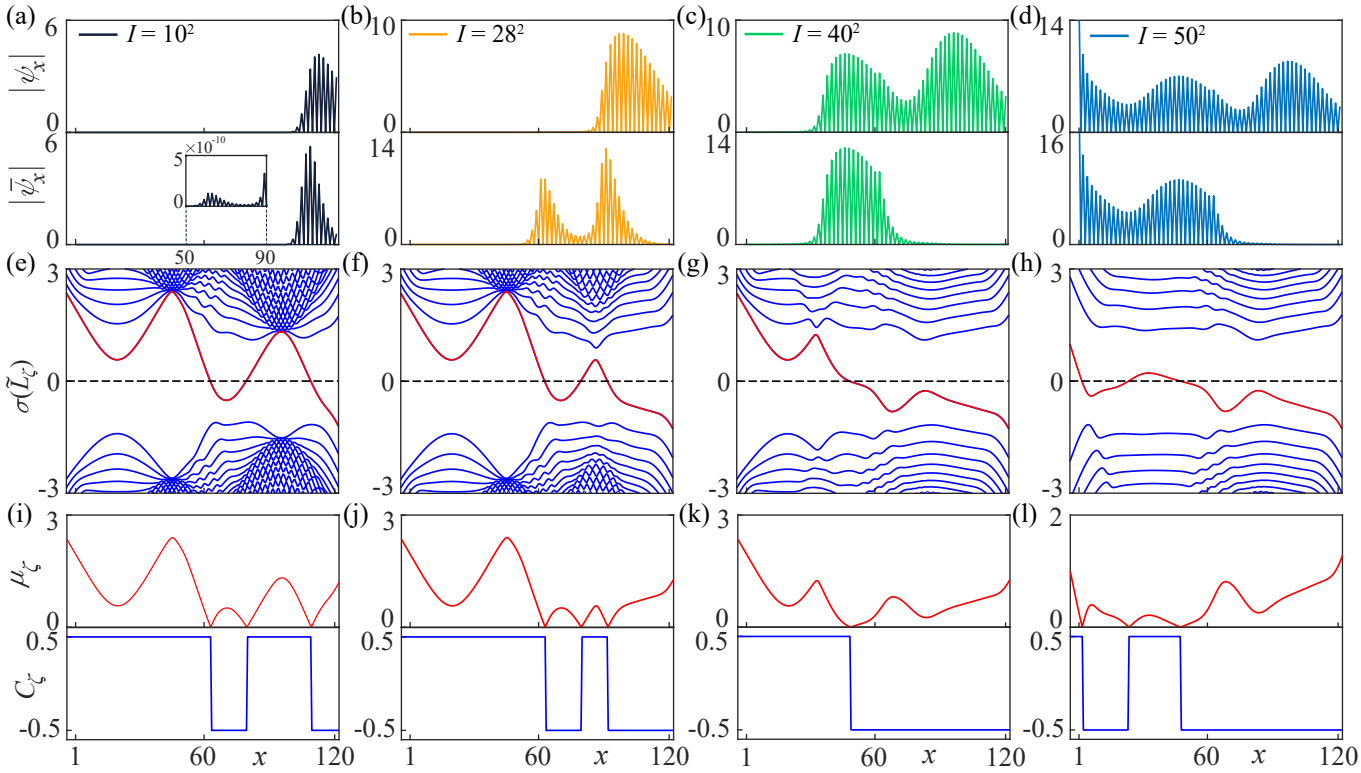

FIG. S7. (a-d) Spatial distribution $|\psi_x|$ of the TZM (upper panel) and their transformed counterparts $|\bar{\psi}_x| = |\hat{S}\psi_x|$ under a similarity transformation (lower panel) for different I. (e-h) Site-resolved eigenvalues $\sigma(\tilde{L}_\zeta)$ of the reduced spectral localizer $\tilde{L}_\zeta$ using the similarity-transformed Hamiltonian $\hat{\mathcal{H}}_S$. (i-l) Site-resolved local gap μ_ζ (upper panels) and topological invariant C_ζ (lower panels) for different I. The distributions of $\tilde{t}_j$ and $\tilde{\lambda}_j$, corresponding to the cosine-shaped TZM, are shown in Fig. S5(d). The pair $\zeta \equiv (x, \bar{\omega})$ is set as $\bar{\omega} = 0$, and $\eta = 0.2$. The other parameters used are $J = 1.5$, $\delta = 0.5$, $\alpha = 0.05$, $\beta = 0.025$, $\tau = t_d = 2.5$, $N = 31$ and $L = 121$.

topological invariant C_ζ (lower panels) are shown in Fig. S7(i-l). For each nonlinear intensity I, as x varies, the local band gap μ_ζ closes, accompanied by a change in the local topological invariant C_ζ. This indicates the presence of a TZM localized near the corresponding x, reflecting the bulk-boundary correspondence. Furthermore, the regions where the local band gap μ_ζ is closest to zero differ for each intensity, signifying the emergence of extended TZMs.

Supplementary Note 7: DETAILS OF EXTENDED TZMS UNDER EXTERNAL PUMPING

A. Dynamical evolution under external pumping

This section provides details on the preparation of TZMs via external pumping. As shown in the main text, nonlinear models can exhibit distinctive dynamical properties that depend on how intensity levels are reached, enabling intrinsic control on TZMs through external pumping. Using the external pumping scheme illustrated in Fig. S8(a), we solve the dynamical evolution equation, shown in the main text, with

$$\frac{\partial |\varphi\rangle}{\partial t} = -i\left(\hat{\mathcal{H}} + \hat{\mathcal{H}}_{\text{loss}}\right)|\varphi\rangle + \xi\,|\mathcal{P}\rangle\, e^{-i\tilde{\omega}t}, \tag{S9}$$

where $\hat{\mathcal{H}}_{\text{loss}} = \sum_j (-i\kappa_a\,|a_j\rangle\langle a_j| - i\kappa_b\,|b_j\rangle\langle b_j|)$, denotes onsite losses in the two sublattices, which contributes to stabilizing the excitation. The pumping sources $|\mathcal{P}\rangle \equiv (0, \cdots, \mathcal{P}_m, \cdots)^T$ are only applied to the a-sites of the non-Hermitian chain [see Fig. S8(a)], with the pumping frequency denoted by $\tilde{\omega}$, and the pumping strength ξ.

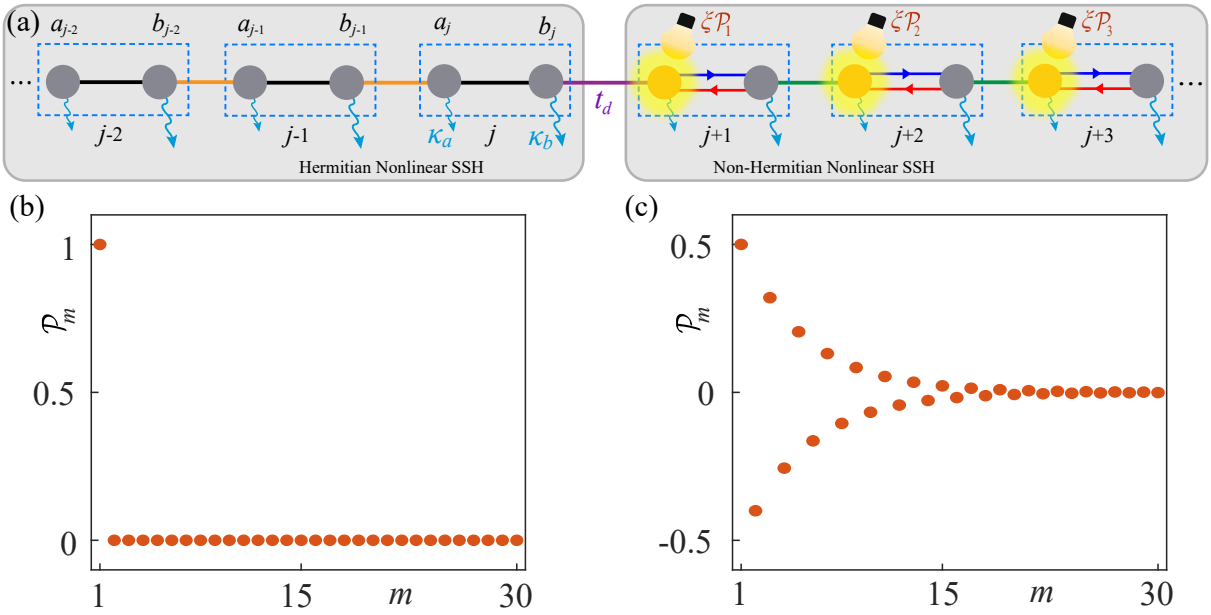

FIG. S8. (a) Schematic showing external pumping applied to the a-sites of the non-Hermitian chain, highlighted by yellow spots. The intensity distributions of pumping sources are represented by $\xi\mathcal{P}_m$, with ξ being pumping strength. The cyan wave arrows indicate onsite losses in the two sublattices, labeled κ_a and κ_b. (b, c) Distributions of two types of pumping sources $|\mathcal{P}_m\rangle$.

Exciting the system initially in the vacuum state at the pumping frequency $\tilde{\omega}$, the evolved steady state $|\Phi\rangle$ from Eq. (S9) satisfies

$$(\hat{\mathcal{H}} + \hat{\mathcal{H}}_{\text{loss}} - \tilde{\omega})\,|\Phi\rangle = -i\xi\,|\mathcal{P}\rangle\,. \tag{S10}$$

Given $\tilde{\omega} = 0$ and $\xi\,|\mathcal{P}\rangle$, the steady state $|\Phi\rangle$ for the excited TZMs can be numerically obtained using a self-consistent method applied to Eq. (S10). We consider two distinct distributions of $\mathcal{P}_m$[10], as shown in Figs. S8(b) and (c).

In the main text, we discussed the excitation of the TZM with a flat wavefunction profile through the external pumping, specifically using a single-site pumping scheme with $\{\mathcal{P}_m\} = \delta_{m,1}$, as shown in Fig. S8(b). Here, we extend our discussion to the realization of other wavefunction profiles by employing a more generalized pumping scheme, as depicted in Fig. S8(c). This approach allows for enhanced control over the spatial structure of the wavefunction[10].

Figure S9(a,e,i,m) presents the intensity distribution $|\Phi|^2$ of the evolved steady state at the resonant pumping frequency $\tilde{\omega} = 0$, plotted as a function of the pumping strength ξ. The results are shown for different target wavefunction profiles: flat (a), square (e), isosceles triangle (i), and cosine (m). The numerical results obtained from the dynamical evolution of Eq. (S9) (black circles) closely match the steady-state solutions (red curves) derived from the self-consistent nonlinear equation Eq. (S10). The corresponding spatial profiles of the evolved steady-state wavefunction $|\text{Re}(\Phi_x)|$ at representative pumping strengths ξ are illustrated in Fig. S9(b,f,j,n). As ξ increases, the wavefunction progressively expands across the entire lattice while retaining the desired spatial profile. Initially, the excitation is localized near the right boundary (not shown here) due to the NHSE, but with increasing pumping strength, the steady-state profile extends leftward (green line), approaching the designed target shape (blue line). Even under strong pumping, the system remains capable of stabilizing into the predefined wavefunction form (purple line) in spite of a more density accumulation at the left boundary.

To further examine the dynamical evolution toward the steady state, figure S9(c,g,k,o) displays the time- and space-resolved evolution of $|\text{Re}(\Phi_x)|$. The steady-state wavefunction profile (red circles) is explicitly highlighted in Fig. S9(d,h,l,p), demonstrating its excellent agreement with the intended target profile (blue line). These results confirm that the external pumping

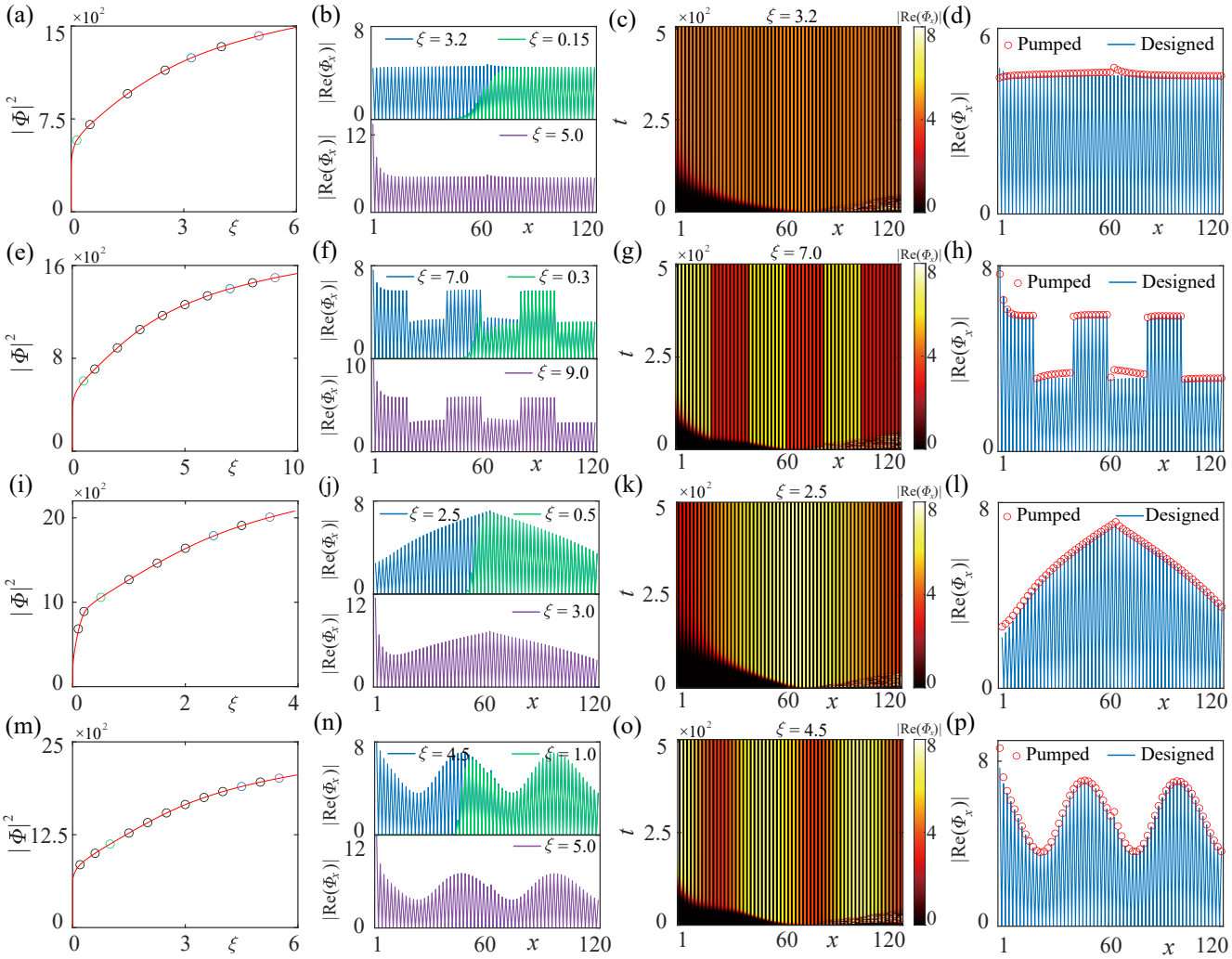

FIG. S9. (a,e,i,m) Intensity $|\Phi|^2$ of the evolved steady state versus ξ for different designed wavefunction profiles with flat (a), square (e), isosceles triangle (i) and cosine shapes (m). The circles represent results from the evolution equation Eq. (S9), which closely match the results (red curve) obtained from the self-consistent nonlinear equation Eq. (S10). (b,f,j,n) Wavefunction profile $|\mathrm{Re}(\Phi_x)|$ of the evolved steady state versus ξ for different designed wavefunction profiles. (c,g,k,o) Time- and space-resolved $|\mathrm{Re}(\Phi_x)|$ for different ξ [the value of ξ marked by the blue circle in (a,e,i,m)]. The corresponding steady-state result is highlighted by red circles in (d,h,l,p). In (d,h,l,p), the steady-state wavefunction profile (red circles) closely matches the designed one (blue line) of the TZM. The distribution of $\mathcal{P}_m$ is shown in Fig. S8 (c). The parameters used are $J = 1.5$, $\delta = 1.0$, $\alpha = \beta = 0.05$, $\tau = t_\mathrm{d} = 2.5$, $\kappa_\mathrm{a} = 0.01$, $\kappa_\mathrm{b} = 0.5$, $\tilde{\omega} = 0$, $N = 31$ and $L = 121$.

effectively drives the system into the designed wavefunction profiles across the entire lattice due to the triple interplay of the nonlinearity, topology and NHSE.

B. Achieving tailored wavefunction profiles with a long-range pattern through external pumping

In this discussion, we explore the ability to excite the targeted extended TZM with a long-range pattern, which could benefit a wide range of topological applications.

For the Hermitian case with $\delta = 0$ and $\beta = 0$, as shown in Fig. S10(a), we present a long-range uniform occupation of the extended TZM over $N = 61$ unit cells in the static lattice. However, it is not possible to fully excite this long-range pattern through external pumping, as shown in Fig. S10(b). Even with a large pumping strength, the left-side lattice sites remain

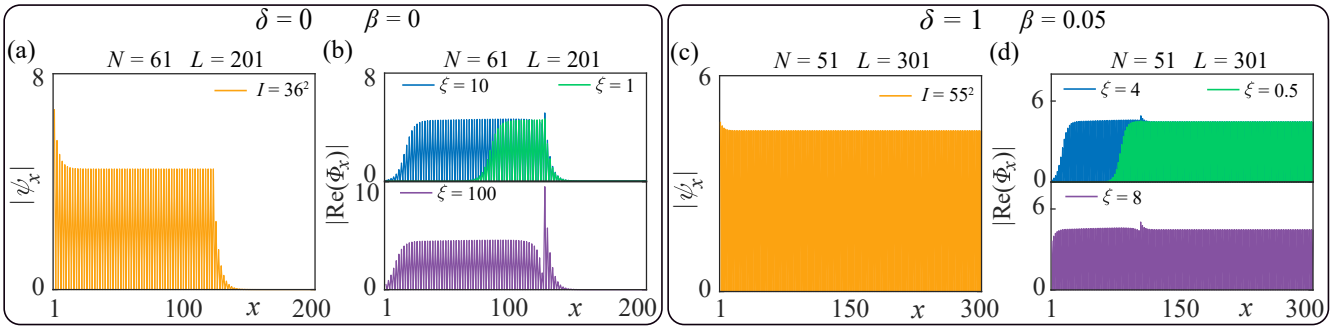

FIG. S10. Hermitian case ($\delta = 0$ and $\beta = 0$): (a) static spatial distributions $|\psi_x|$ of the extended TZM in a long lattice, and (b) Wavefunction profiles $|\mathrm{Re}(\Phi_x)|$ of the evolved steady states under external pumping at a single site located at $2N + 1$ with $\tilde{\omega} = 0$, in accordance with the static results in (a). Non-Hermitian case ($\delta = 1$ and $\beta = 0.05$): (c) static spatial distributions $|\psi_x|$ of the extended TZM in a long lattice, and (d) Wavefunction profiles $|\mathrm{Re}(\Phi_x)|$ of the evolved steady states under external pumping at a single site located at $2N + 1$ with $\tilde{\omega} = 0$, in accordance with the static results in (c). The parameters used are $J = 1.5$, $\tau = t_\mathrm{d} = 2.5$, $\tilde{t}_j = 1.5$, and $\alpha = 0.05$, with $\tilde{\lambda}_j = 2.5$ for (a,b) and $\tilde{\lambda}_j = 1.5$ for (c,d).

unexcited. In contrast, for the non-Hermitian case, such as for $\delta = 1$ and $\beta = 0.05$, as shown in Fig. S10(c,d), we can readily excite a long-range uniform occupation of the extended TZM over a much larger number of unit cells. This highlights the significant influence of the interplay between nonlinearity and non-Hermitian dynamics, which facilitates the excitation of extended modes over a much broader range compared to the Hermitian case.

* E-mail: liutao0716@scut.edu.cn

[1] A. Bisianov, M. Wimmer, U. Peschel, and O. A. Egorov, "Stability of topologically protected edge states in nonlinear fiber loops," Phys. Rev. A **100**, 063830 (2019).

[2] K. Sone, M. Ezawa, Z. Gong, T. Sawada, N. Yoshioka, and T. Sagawa, "Transition from the topological to the chaotic in the nonlinear Su–Schrieffer–Heeger model," Nat. Commun. **16**, 422 (2025).

[3] Y. Hadad, J. C. Soric, A. B. Khanikaev, and A. Alù, "Self-induced topological protection in nonlinear circuit arrays," Nat. Electron. **1**, 178 (2018).

[4] X. Guo, L. Jezequel, M. Padlewski, H. Lissek, P. Delplace, and R. Fleury, "Practical realization of chiral nonlinearity for strong topological protection," arXiv:2403.10590 (2024).

[5] J. Wu, R.-C. Shen, L. Zhang, F. Chen, B. Wang, H. Chen, Y. Yang, and H. Xue, "Nonlinearity-induced reversal of electromagnetic non-Hermitian skin effect," arXiv:2505.09179 (2024).

[6] T. Helbig, T. Hofmann, S. Imhof, M. Abdelghany, T. Kiessling, L. W. Molenkamp, C. H. Lee, A. Szameit, M. Greiter, and R. Thomale, "Generalized bulk–boundary correspondence in non-Hermitian topolectrical circuits," Nat. Phys. **16**, 74 (2020).

[7] C.-X. Guo, L. Su, Y. Wang, L. Li, J. Wang, X. Ruan, Y. Du, D. Zheng, S. Chen, and H. Hu, "Scale-tailored localization and its observation in non-Hermitian electrical circuits," Nat. Commun. **15**, 9120 (2024).

[8] T. Liu W. Ju H. Wang, J. Liu, "Observation of impurity-induced scale-free localization in a disordered non-Hermitian electrical circuit," Front. Phys. **20**, 14203 (2025).

[9] S. Yao and Z. Wang, "Edge states and topological invariants of non-Hermitian systems," Phys. Rev. Lett. **121**, 086803 (2018).

[10] K. Bai, J.-Z. Li, T.-R. Liu, L. Fang, D. Wan, and M. Xiao, "Arbitrarily configurable nonlinear topological modes," Phys. Rev. Lett. **133**, 116602 (2024).